First-principles study on the stability and work function of low-index surfaces of TiB$_2$

Qian Wang[a,b], Changzhi Liu[c], Ruijuan Yao[c], Hong Zhu[b,d], Xiaomin Liu[a], Mingliang Wang[a,*], Zhe Chen[b,*], Haowei Wang[a,b]

[a] School of Materials Science and Engineering, Shanghai Jiao Tong University, Shanghai 200240, China
[b] State Key Laboratory of Metal Matrix Composites, Shanghai Jiao Tong University, Shanghai 200240, China
[c] Beijing Institute of Astronautical Systems Engineering, Beijing 100076, China
[d] University of Michigan – Shanghai Jiao Tong University Joint Institute, Shanghai Jiao Tong University, Shanghai 200240, China

ARTICLE INFO

ABSTRACT

The structures, electronic properties, surface energies and work functions of low-index surfaces of TiB$_2$ compound are studied using the first-principles calculations based on density functional theories. The structural relaxations and electronic properties show that the Ti-terminated (0 0 0 1) and (1 0 $\bar{1}$ 0) surfaces are more stable than the corresponding B-terminated surfaces, and the (1 1 $\bar{2}$ 0) surface is the most stable surface of all surfaces. Through the comparison of surface energies, it can be obtained that the Ti-terminated (0 0 0 1) and (1 0 $\bar{1}$ 0) surfaces are thermodynamically more favorable under Ti-rich condition, and B-terminated (0 0 0 1) surface is thermodynamically more favorable under B-rich condition. Therefore, the morphologies of TiB$_2$ particles consisting of (0 0 0 1) and (1 0 $\bar{1}$ 0) surfaces are related to the atomic concentration in the melt. In addition, the B-terminated (0 0 0 1) surface has the largest work function among all surfaces.

1. Introduction

As a typical transition-metal diboride (TMB$_2$), Titanium diboride (TiB$_2$) has many spectacular properties, such as elevated Young's modulus, improved hardness, superior specific strength, and high chemical stability [1]. Therefore, it has been widely used as the reinforcing phase in metal matrix composites, grain refiner in Al alloys, cutting tools, wear resistant coating and so on [2–4]. The morphology of TiB$_2$ particles in those materials has a significant impact on their physical and chemical properties, but is difficult to be controlled [5]. In pure Al, TiB$_2$ particles generally exhibit a hexagonal plate-like morphology [6]. Based on Abdel-Hamid's analysis [7], it was found the growth of these plate-like particles was limited by large (0 0 0 1) faces and smaller (1 0 $\bar{1}$ 0) facets, and their growth morphology was similar to the theoretical growth morphology calculated from the attachment energies of crystal faces. Then, Hyman et al. [8] reported that as the B content increases, the TiB$_2$ particles in Ti-A1 alloys should gradually change from a highly curled sheet to a needles, plates and equiaxed particles. Subsequently, Li et al. [5] fabricated the TiB$_2$ particles in different reaction temperature and claimed that the single crystal of hexagonal plate-like TiB$_2$ microcrystals exhibited hierarchical tower-like and

dendritic morphologies when the atomic concentration, reaction rate and atomic diffusion rate were high in the melt. However, there are currently lacking theoretical verifications on these viewpoints.

In recent years, computational materials science has been widely applied to TMB$_2$ research with the rapid development of computing hardware and software [9]. A large number of works focused on the structural and physical properties of bulk diborides have been published [10–13]. Former results proved that the bulk TiB$_2$ had the mixture characteristics of the covalent, ionic and metallic bonds among B and Ti atoms [14,15]. More recently, many researchers paid their attention to the (0 0 0 1) surface. For example, Han et al. [16] calculated the Ti- and B- terminated TiB$_2$ (0 0 0 1) surfaces, and claimed that Ti-terminated (0 0 0 1) surface was more thermodynamically favorable. Yamamoto et al. [17–19] compared the atomic and electronic structures of TaB$_2$ (0 0 0 1), WB$_2$ (0 0 0 1) and HfB$_2$(0 0 0 1) surfaces by both experiments and calculations, and found that the B-terminated TaB$_2$ (0 0 0 1), WB$_2$ (0 0 0 1) surfaces and Hf-terminated HfB$_2$ (0 0 0 1) surface were more stable than other terminated surfaces. Furthermore, they claimed that it may be a general rule in Group-IV diborides that the TM-terminated (0 0 0 1) surface is more stable than the B-terminated surface. Subsequently, Zhang et al. [20] also agreed with this

opinion, since they investigated the bonding and electronic structures of ZrB_2 (0 0 0 1) surface, and found that the Zr-terminated (0 0 0 1) surface was thermodynamically more favorable than the B-terminated surface. Nevertheless, most current calculation studies only focused on the (0 0 0 1) surface properties of TMB_2. Other low-index surface properties of TMB_2 are rarely reported to the best of our knowledge.

Based on the above discussions, the study of low-index surfaces of TiB_2 compound is not only important to further clarify the formation mechanism of TiB_2 particles and then to control their morphology, but also provides a reference for the relative calculation of other borides. Therefore, combined the attachment energies for various low-index facets of TiB_2 crystal [7] and surface model method of the plane slab, we studied the structures, electronic properties, surface energies and work functions of low-index surfaces (i.e., (0 0 0 1), (1 0 $\bar{1}$ 0) and (1 1 $\bar{2}$ 0)) of TiB_2 compound by first-principles calculations in the present investigation.

2. Computational details

In the present work, the density functional theory (DFT) calculations were performed in the Vienna Ab initio Simulation Package (VASP) with projected augmented wave (PAW) pseudopotentials and a plane-wave basis set [21–23]. The Perdew-Burke-Ernzerhof (PBE) exchange–correlation functional [24] within the generalized gradient approximation (GGA) were applied. The detailed information for the selection of calculation parameters are shown at Part 1 of Supplemental Materials. According to the convergence test (Fig. S1), all calculations were performed with a plane-wave cutoff energy of 450 eV when the convergence of the energy differences was within 2 meV/atom. The self-consistency convergence criterion for energy tolerance was set to 10^{-6} eV/atom. Comparing the energy differences in Fig. S2, the $22 \times 22 \times 22$ k-point meshes for the bulk unit cell and $22 \times 22 \times 1$ k-point meshes for the surface supercell were employed with convergence within 2 meV/atom. Additionally, the k-space integration for Brillouin zone sampling has been constructed using Gamma centered grids. The valence electrons for the adopted pseudopotentials of B and Ti atoms were $2s^2 2p^1$ and $3s^2 3p^6 3d^2 4s^2$, respectively. The conjugate gradient algorithm was applied to relax atomic structures to their instantaneous ground state by minimizing Hellman- Feynman forces until the total force on each ion was converged to 0.01 eV/Å [25]. A vacuum layer of 1.0 nm thickness has been added in each surface supercell to prevent unwanted interactions between the slab and its periodic arrangement along the surface normal direction. The low-index surfaces of TiB_2 compound (i.e., (0 0 0 1), (1 0 $\bar{1}$ 0) and (1 1 $\bar{2}$ 0) surfaces) have been studied.

3. Results and discussions

3.1. Bulk properties

The structure and electronic properties of bulk TiB_2 are shown in Fig. 1.The crystal structure of AlB_2-type TiB_2 belongs to the P6/mmm space group. In detail, a close-packed hexagonal Ti layer and a graphite-like B layer have been arranged alternately along the c axis inside the unit cell. This unit cell owns one chemical formula unit, in which Ti and B atoms take the sites 2d (0.333, 0.667, 0.5) and 1a (0, 0, 0) within the Wyckoff system, respectively (Fig. 1a). According to the Ti-B phase diagram [26], the pure Ti (P63/mmc) and β-B (R-3 M) were selected for calculations. Table 1 shows the optimized lattice constants acquired from the bulk simulations, which are in good agreements with the experimental [27–30] and other theoretical [31–33] results.

The formation energy of TiB_2 is adopted to evaluate the phase stability, which can be calculated using the following equation:

$$\Delta H_f^0(TiB_2) = E_{TiB_2}^{bulk} - E_{Ti}^{bulk} - 2E_B^{bulk} \tag{1}$$

where $\Delta H_f^0(TiB_2)$ is the formation energy of the TiB_2 bulk; $E_{TiB_2}^{bulk}$ is the ground state energy of the optimized structure of TiB_2; E_{Ti}^{bulk} and E_B^{bulk} are the ground state energies of the individual atoms in the corresponding elemental bulk states. The calculated formation energy of TiB_2 is −3.237 eV (Table 1), which means the TiB_2 phase is stable with respect to the elemental states.

The density of state (DOS) spectrum (Fig. 1b) and valence charge density map (Fig. 1c) are calculated for the bulk TiB_2. In Fig. 1b, the total DOS (TDOS) and partial DOS (PDOS) of TiB_2 from − 13 to 6 eV are plotted, and the Fermi energy (E_F) is set to zero. Form TDOS, three main peaks and one pseudogap around the Fermi level can be clearly observed. The peak located at −9.8 eV belongs to the bonding state, and it is mainly associated with the B 2s and B 2p hybridization shown in PDOS spectrum of B atoms. The peak located at −3.3 eV indicates the bonding or the hybridization of Ti 3d and B 2p orbitals, as indicated by PDOS spectra of Ti and B atoms. Moreover, the peak located at 2.8 eV belongs to the antibonding states of TiB_2. The locations of these peaks and their associated status are consistent with other literature [14,15]. Furthermore, the pseudogap around E_F is mainly due to the Ti-B hybridization [10]. Additionally, the pseudogap and a lower DOS at the Fermi energy altogether demonstrate the excellent stability of TiB_2 over other titanium borides [34]. In Fig. 1c, two B atoms have a dumbbell-like B-B atomic pair, which clearly originates from the B-B covalent bond formed by sp^2 hybridized orbitals (Fig. 1b). Moreover, the valence charge density between Ti and B atoms is also large, which obviously creates by the Ti-B covalent bond formed by hybridization of B 2p and Ti 3d orbitals (Fig. 1b) [14].

3.2. Surface convergence

In order to ensure the bulk-like character interiors, the low-index surface slab model should be thick enough. Thus, the convergence test on the slab is performed. Firstly, in consideration of the structural symmetry, the surface slab models can be constructed as shown in Fig. 2, in which, Fig. 2(a1) is nonstoichiometric Ti-terminated (0 0 0 1) surface, Fig. 2(a2) is nonstoichiometric B-terminated (0 0 0 1) surface, Fig. 2(b1) is nonstoichiometric Ti-terminated (1 0 $\bar{1}$ 0) surface, Fig. 2(b2) is nonstoichiometric B-terminated (1 0 $\bar{1}$ 0) surface and Fig. 2(c) stoichiometric (1 1 $\bar{2}$ 0) surface. Then, the convergence of the low-index surfaces slab was tested according to the change of interlayer spacing $\triangle d_{i,i+1}$ (i = 1–5) [33], as shown in the following equation:

$$\Delta d_{i,i+1} = \frac{d_{i,i+1} - d_0}{d_0} \times 100\% \tag{2}$$

where $\triangle d_{i,i+1}$ is the interlayer spacing between the i_{th} and $(i + 1)_{th}$ layers after relaxation; d_0 is the interlayer spacing before relaxation. In this equation, a positive $\triangle d_{i,i+1}$ means an interlayer extension, while a negative value indicates an interlayer contraction.

Tables S2–S4 have exhibited the convergence testing results at Part 2 of Supplemental Materials. In Table S2, the relaxation results of (0 0 0 1) slabs are dependent on the termination and slab thickness. When the outermost layer is defined as the first layer, the variation in the layer spacing is mainly concentrated at the outermost two layers (Table S2). For the Ti-(0 0 0 1) slab, when the slab thickness is more than nine layers, the slab model possesses a bulk-like interior. Similarly, for the B-(0 0 0 1) slab consisting of nine layers, its interior exhibits excellent bulk-like structural characteristics. Therefore, the nine-layer Ti-terminal or B-terminal (0 0 0 1) slabs are selected for further calculations and analyses (Fig. 2a)

The relaxation results of Ti-(1 0 $\bar{1}$ 0) and B-(1 0 $\bar{1}$ 0) slabs are listed in Table S3. Due to a complex structure of the polar (1 0 $\bar{1}$ 0) surface, only three slabs of different thicknesses are relaxed. From the results, we can find that the change of interlayer distance in the slab interior is negligible within a nineteen-layer Ti-(1 0 $\bar{1}$ 0) slab or a seventeen-layer B-(1 0 $\bar{1}$ 0) slab. Thus, the nineteen-layer Ti-terminal and seventeen- layer
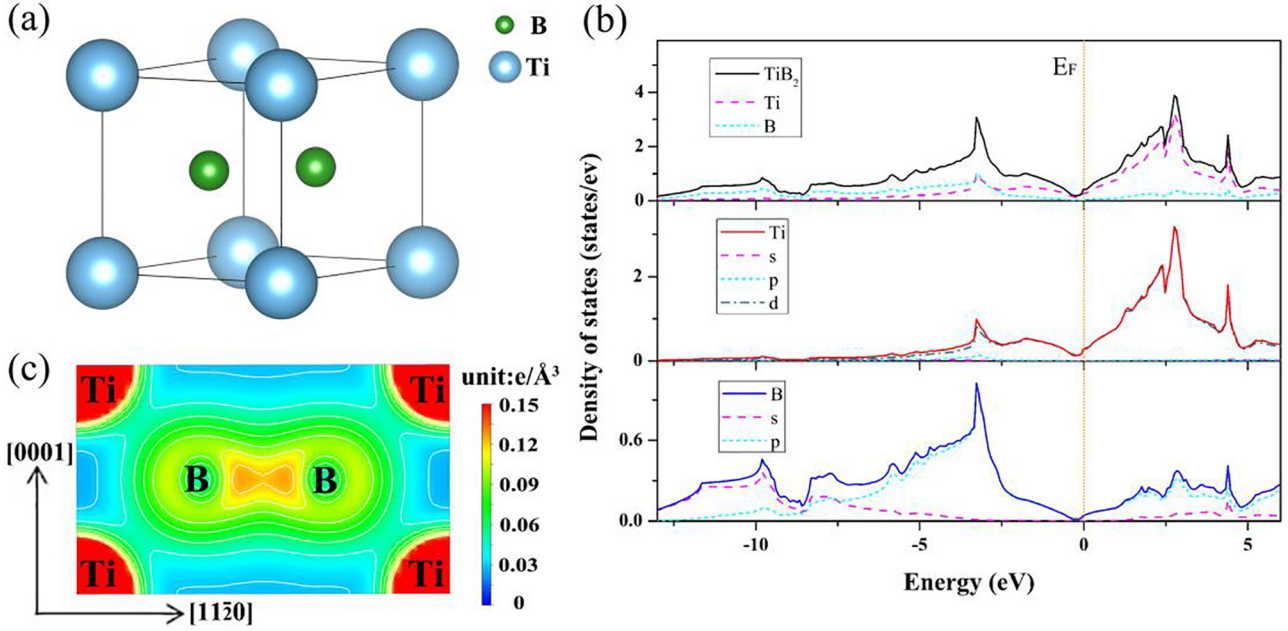
Fig. 1. Structural and electronic properties of bulk TiB$_2$: (a) the unit cell; (b) the TDOS and PDOS of bulk TiB$_2$; (c) distribution of valence charge density on the (1 1 $\bar{2}$ 0) plane (The electron density contours are displayed from 0 to 0.15 e/Å^3).

B-terminal (1 0 $\bar{1}$ 0) slabs are used in this work (Fig. 2b). The relaxation results of (1 1 $\bar{2}$ 0) slabs with thickness ranging from 3 to 9 layers are listed in Table S4, in which the slabs with more than seven atomic layers possess a bulk-like interior. Therefore, the seven-layer (1 1 $\bar{2}$ 0) slab is adopted here (Fig. 2c).

3.3. Surface relaxation

In order to quantitatively compare the atomic relaxation process in detail, the following parameters are used to analyses. Firstly, Δz and δz are used to depict the relaxation of each atom normal to the surface, and estimated by the following equations, respectively.

$$\Delta z = z_i^{relaxed} - z_i^{unrelaxed} \tag{3}$$

$$\delta z = \frac{\Delta Z}{d_0} \times 100\% \tag{4}$$

where $z^{unrelaxed}$ and $z^{relaxed}$ are the atomic positions of i_{th}-layer Ti or B atom along z-axis before and after the relaxation. Hence, a positive value of Δz or δz means that the atoms move toward the vacuum. Similarly, a negative value means that the atoms move toward the inner atomic layers.

Secondly, r_i is used to illustrate the rumpling phenomenon caused by simultaneously relaxing different atoms on the same layer and expressed as:

$$r_i = \frac{z_i^{Ti} - z_i^{B}}{d_0} \times 100\% \tag{5}$$

where z_i^{Ti} and z_i^{B} are the average atomic positions of Ti and B atoms on the i_{th} layer after relaxation, respectively.

The atomic relaxation results of the five layers in the surface slab are shown in Fig. 3, and relevant data are respectively listed in Tables S5–S9 at Part 3 of Supplemental Materials. From Fig. 3a and b, each layer of Ti- or B-(0 0 0 1) surface only contains one type of atom, and the Ti or B atomic layer is alternately arranged. Therefore, there is no rumpling phenomenon in the nonstoichiometric (0 0 0 1) surface [10]. Correspondingly, the r_i values are all zero in Tables S5 and S6.

In Table S5, the atomic relaxation results of the Ti-(0 0 0 1) surface are listed. For δz, only the outermost layer has a large negative value (-3.57%), while the other layers are all minor positive values which are smaller than 2.00%. Thus, only the Δz of the outmost layer is shown in Fig. 3a. Meanwhile, the interlayer spacings $\Delta d_{i, i+1}$ also have the analogous trend. The Δd_{12} shrinks more than 4.70%. However, all other layer spacings extend by less than 0.50%. Therefore, the relaxation of Ti-(0 0 0 1) surface is mainly focused on the outmost layer.

The atomic relaxation results of B-(0 0 0 1) surface are shown in Table S6. The B atom in the first layer moves toward the inner layer by ~3.57%, while the Ti atom in the second layer moves to the vacuum layer by ~3.40%. Others are all smaller than 1.00%. Furthermore, the interlayer spacings $\Delta d_{i, i+1}$ also have a similar trend. In Table S6, Δd_{12} of B-(0 0 0 1) surface is -6.70%, Δd_{23} is 2.59%, and other interface

Table 1
Calculated lattice parameters and ground-state energies of the bulk Ti, B and TiB$_2$ along with previous theoretical and experimental values.

Crystal	Structure	a (Å)	b (Å)	c (Å)	Formation energy (eV/cell)	References
Ti	P63/mmc	2.937	2.937	4.645		This work
		2.951	2.951	4.684		Experiment [27]
		2.933	2.933	4.657		Theory [31]
B	R-3M	10.116	10.116	10.116		This work
		10.170	10.170	10.170		Experiment [28]
		10.145	10.145	10.145		Theory [32]
TiB$_2$	P6/mmm	3.034	3.034	3.224	-3.237	This work
		3.032	3.032	3.229	-3.401	Experiment [29,30]
		3.030	3.030	3.221	-3.256	Theory [33]
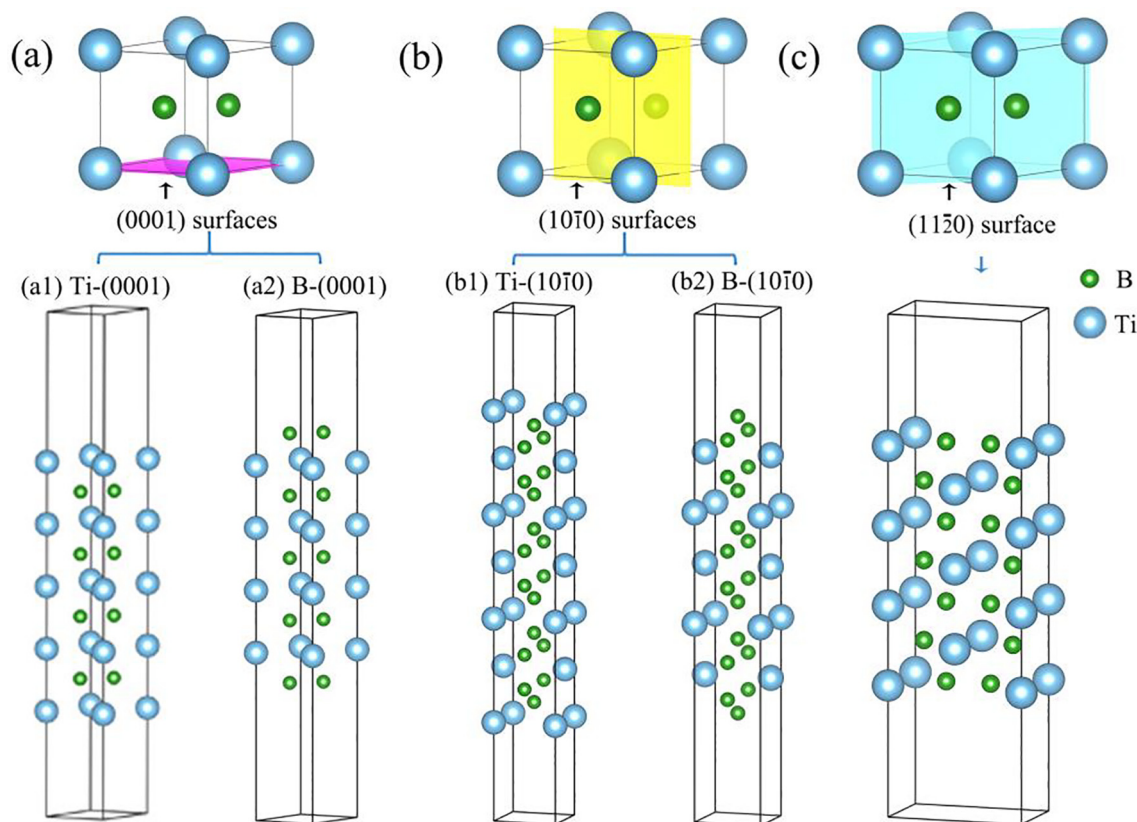
Fig. 2. Calculation models of low-index surface structures of TiB_2: (a1) Ti-(0 0 0 1), (a2) B-(0 0 0 1), (b1) Ti-(1 0 $\bar{1}$ 0), (b2) B-(1 0 $\bar{1}$ 0) and (c) (1 1 $\bar{2}$ 0).

spacings are all smaller than 0.50%. Comparing the calculation results in Tables S5 and S6, it is concluded that the relaxation mainly appears on the outmost two layers. Additionally, the relaxation of Ti-(0 0 0 1) surface is obviously smaller than B-(0 0 0 1) surface. This feature is also consistent with the opinion proposed by Han et al. [16] that the TM terminated surface in the group-IV TMB_2 is more stable.

For nonstoichiometric (1 0 $\bar{1}$ 0) surface, the atomic structure of the five layers on the Ti terminal surface is different from the B terminal surface (Fig. 3c and d). Combined with the calculation model in Fig. 2b, we can find seven Ti atom layers and twelve B atom layers are included in nineteen-layer Ti-(1 0 $\bar{1}$ 0) surface (Fig. 2b1), while five Ti atom layers and twelve B atom layers are listed on seventeen-layer B-(1 0 $\bar{1}$ 0) surface (Fig. 2b2). Therefore, the B terminal surface has a small amount of Ti atomic layer (Fig. 3d). The detailed calculation results of the structural relaxation for nonstoichiometric (1 0 $\bar{1}$ 0) surfaces are given in Tables S7 and S8.

In Table S7 for the Ti-(1 0 $\bar{1}$ 0) surface, all atoms have negative δz values. The first layer atom even moves up to -15.96%, and other layers are all smaller than 5.00%. The Δz of the outmost layer is shown in Fig. 3c. Then, the interlayer spacings of the outermost two layers (Δd_{12}) and the innermost two layers (Δd_{56}) are reduced, whereas the others are increased. Especially, the interlayer spacing Δd_{12} in Table S7 is -15.60%, which is about three times larger than that in Table S5 for the Ti-(0 0 0 1) surface. The other interlayer spacings for Ti-(1 0 $\bar{1}$ 0) surface are all smaller than 1.80%.

In Table S8 for the B-(1 0 $\bar{1}$ 0) surface, all atoms move to the inner layer except for the second layer B atom moving toward the vacuum. The movement (δz) of the first layer is even larger than -34.12%, the second layer is 2.06%, the third layer is -10.29%, and other layers are all smaller than 5.30%. Additionally, the interlayer spacings of Δd_{12}, Δd_{34}, and Δd_{56} are reduced, whereas Δd_{23} and Δd_{45} are increased. It is worth noting that the outermost interlayer spacing Δd_{12} shrinks by $\sim 36.18\%$, while Δd_{23} extends by $\sim 12.39\%$. Therefore, the structural

changes before and after the relaxation of B-(1 0 $\bar{1}$ 0) surface is larger than Ti-terminated. This finding is similar to the (0 0 0 1) surface, although there is no other theoretical data which can be compared.

For the stoichiometric (1 1 $\bar{2}$ 0) surface, the surface structure where each layer simultaneously contains Ti and B atoms is displayed in Fig. 3e. The r_i value is used to estimate the degree of the rumpling phenomenon, which is listed in Table S9. From the calculated results, the δz values of other atoms are positive and larger than 0.50% except for the B atom in the outermost layer. That is to say, the outermost B atoms move toward the vacuum layer, and the other atoms move toward the inner layer after the relaxation. It also means the Ti atom in the outermost layer is easier to move than the B atom, which has resulted in a significant rumpling phenomenon on this surface (Fig. 3e). Furthermore, the outermost interlayer spacing is compressed, and the second interlayer spacing is enlarged. However, the values of all interlayer spacings are all smaller than 2.00%. Overall, the structure of (1 1 $\bar{2}$ 0) surface is more stable than other surfaces after structure relaxation.

3.4. Surface electronic properties

3.4.1. Density of states

The TDOS and PDOS of the low-index surface structures of TiB_2 are calculated and plotted in Fig. 4 to reveal the electronic structures. In the DOS for Ti-(0 0 0 1) surface (Fig. 4a), the enhancement of TDOS at Fermi energy (E_F) can be clearly observed, which is the only difference from the bulk TiB_2. Further combined with the PDOS spectra of atoms in different layers, it is shown that the contribution by the hybridization of Ti $3d$ and B $2p$ orbitals, especially the electrons from Ti orbital in the first layer play a major role. Thus, Ti-(0 0 0 1) surface has exhibited metallic property. Moreover, the PDOS spectrum of Ti atom located on the third layer is different from that on the first layer, which may be caused by the formation of the surface state in the slab. Such similar
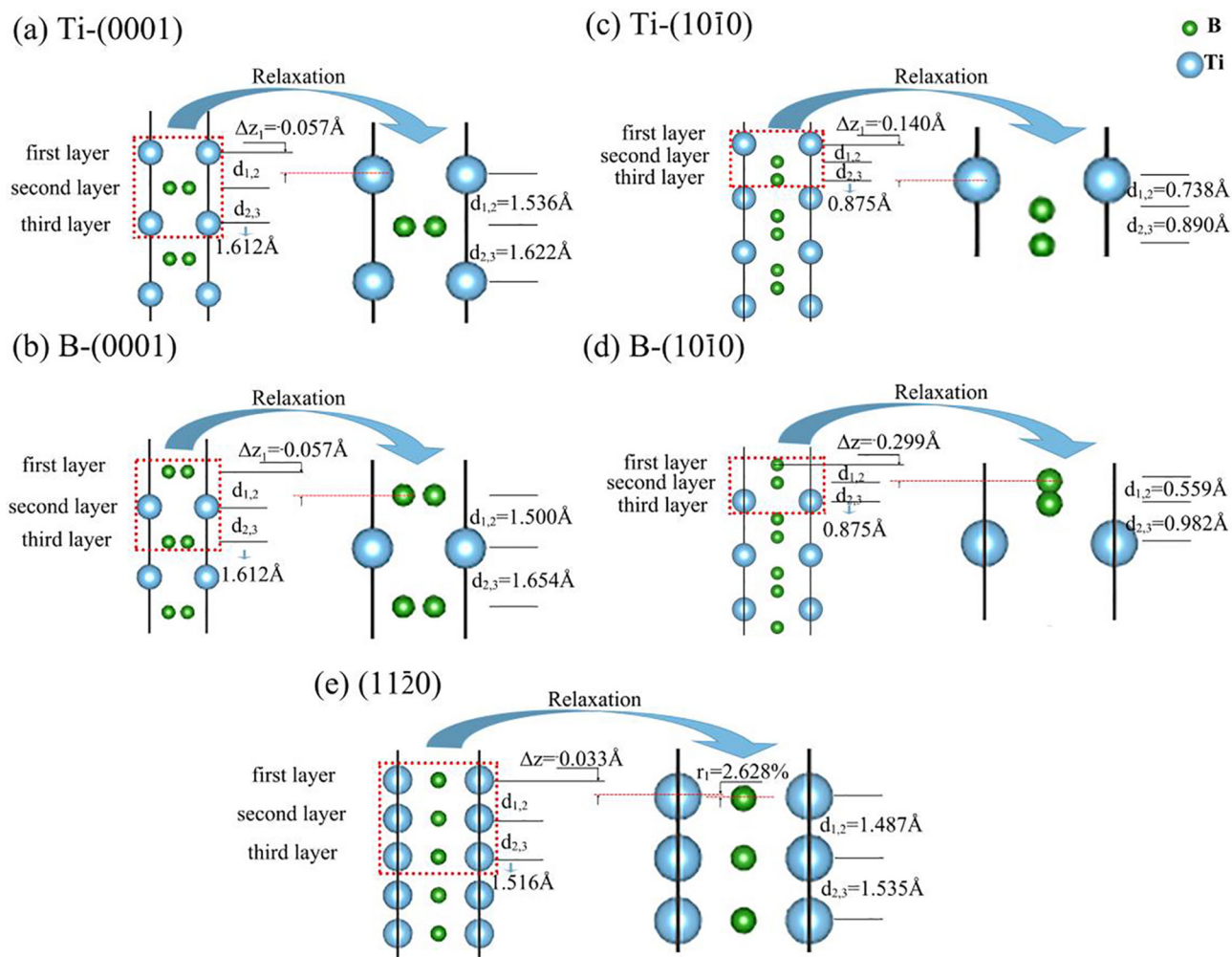
Fig. 3. Surface relaxations of (a) Ti-(0 0 0 1), (b) B-(0 0 0 1), (c) Ti-(1 0 $\bar{1}$ 0), (d) B-(1 0 $\bar{1}$ 0) and (e) (1 1 $\bar{2}$ 0).

characters can also be observed in the low-index surfaces of Al_3Sc or Al_3Ni intermetallics [35,36]. In the DOS for B-(0 0 0 1) surface (Fig. 4b), a maximum DOS value appears near the Fermi level. According to the PDOS spectra of the top four layers, this enhancement is mainly attributed to the B $2p$ orbital and Ti $3d$ orbital located on first and second layers, accordingly. Therefore, the B-(0 0 0 1) surface also displays a metallic character. Furthermore, the PDOS spectra of atoms in the inner two layers are similar to those in the bulk (Fig. 1c). However, they are different from those in the outmost two layers. As a result, the formation of the surface state affects the outermost two layers of the B-(0 0 0 1) surface.

For the DOS of Ti-(1 0 $\bar{1}$ 0) surface (Fig. 4c), the Fermi level shifts to the right in comparison with the bulk TiB_2 (Fig. 1c). Herein, the larger enhancement of the TDOS on Fermi level is mainly derived from the Ti $3d$ orbital in the first layer, which is the same as the Ti-(0 0 0 1) surface. Moreover, the PDOS spectra of either Ti or B atoms are quite different from those in bulk TiB_2 (Fig. 1c), which may be caused by the formation of the surface state in the slab. For the DOS of B-(1 0 $\bar{1}$ 0) surface (Fig. 4d), the smaller enhancement of TDOS spectra on the Fermi level is owing to the interaction of the two layers of B $2p$ orbitals and the third layer of Ti $3d$ orbital. The PDOS of B atom in the first layer has an abnormal peak near the E_F, caused by the absence of Ti atom on the surface.

The DOS spectra of the top two layers in non-polar (1 1 $\bar{2}$ 0) surface are given in Fig. 4e. Since each layer of the surface contains one Ti and two B atoms, the electronic structure is relatively similar. Compared with the TDOS of bulk TiB_2 (Fig. 1c), the Fermi level moves to the left.

Combined with PDOS spectra, the surface B-$2p$ and Ti-$3d$ electrons move towards Fermi level, leading to an increase in the metallic property and a decrease in stability. Moreover, the E_F enhancement in TDOS is mainly due to the contribution of the Ti atom in the first layer.

Based on the above discussion, all surfaces exhibit metallic properties, which are the same as the bulk TiB_2 (Fig. 1c). Furthermore, the surface states in DOS spectra disappear quickly for the Ti-terminated (0 0 0 1) or (1 0 $\bar{1}$ 0) surfaces, and slowly disappear for the B-terminated surfaces. Remarkably, a similar phenomenon is also observed in the ZrB_2 (0 0 0 1) surface [20].

3.4.2. Charge density map

To further analyze the electronic structure of the surfaces, the contour maps of charge density difference are also calculated and displayed in Fig. 5. In the charge density difference for Ti-(0 0 0 1) surface (Fig. 5a), the charge accumulations can be clearly observed in the interlayer region between the top two layers, especially on the first Ti atoms layer. In the meantime, fewer charge depletions occur in the vacuum. In the charge density difference for B-(0 0 0 1) surface (Fig. 5b), the significant charge accumulations appear on the outmost two layers. As a result, the interlayer Ti-B chemical bonds are reinforced, and the outermost interlayer spacings in Tables S5 and S6 are decreased in accompany. Additionally, the degree of charge transformation in B-(0 0 0 1) surface is obviously larger than that in Ti-(0 0 0 1) surface, so the outermost interlayer spacing Δd_{12} in Table S6 is larger than that in Table S5. These phenomena can be well compared with other theoretical works [37,38].
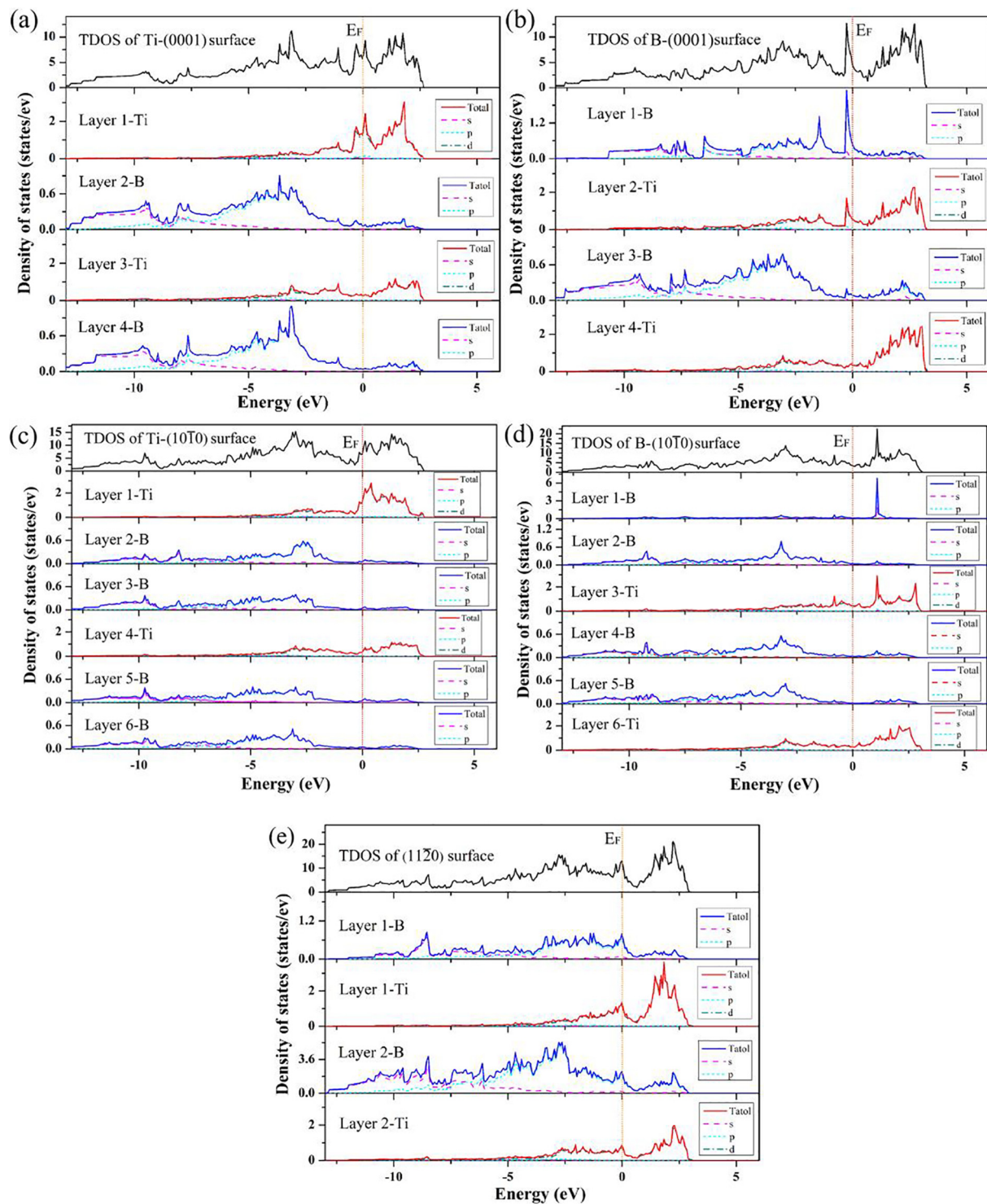
Fig. 4. TDOS and layered PDOS of low-index surfaces of TiB$_2$: (a) Ti-(0 0 0 1), (b) B-(0 0 0 1), (c) Ti-(1 0 $\bar{1}$ 0), (d) B-(1 0 $\bar{1}$ 0) and (e) (1 1 $\bar{2}$ 0).

In the charge density difference map for Ti-(1 0 $\bar{1}$ 0) surface (Fig. 5c), the Ti atom in the first layer has a little charge accumulation. Meanwhile, the little charge depletion in the vacuum is also observed, which is like Ti-(0 0 0 1) surface. However, for B-(1 0 $\bar{1}$ 0) surface (Fig. 5d), the B atom in the first layer has extreme charge accumulation, and the vacuum layer has the obvious charge depletion. Comparing the calculation results in Fig. 5c and d, it is certain to say the difference of electron concentration at the outermost layer of the B terminal is more serious than Ti terminal.

The charge density difference map of the non-polar (1 1 $\bar{2}$ 0) slab on the (2 1 $\bar{3}$ 0) plan is shown in Fig. 5e. Unlike other surfaces, there is no evident charge accumulation on the outermost layer in the slab, and only a small amount of charge is depleted in the vacuum layer. This phenomenon is consistent with the relaxation results in Table S9.

According to the above discussion, the charge accumulation should mainly locate in the outmost layer, and the charge depletion in vacuum for the B-terminated polar surfaces is much larger than those for the Ti-terminated. However, the charge transformation is truly slight in non-
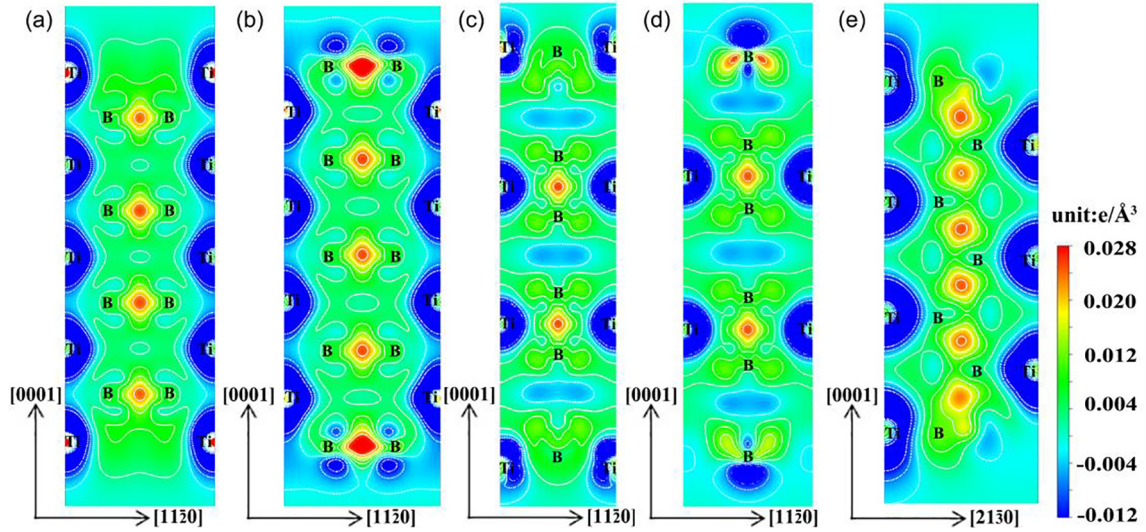
Fig. 5. Charge density difference maps of low-index surfaces of TiB$_2$, including (1 1 $\bar{2}$ 0) planes for (a) Ti-(0 0 0 1), (b) B-(0 0 0 1), (c) Ti-(1 0 $\bar{1}$ 0), (d) B-(1 0 $\bar{1}$ 0), and (2 1 $\bar{3}$ 0) plan for (e) (1 1 $\bar{2}$ 0).

polar (1 1 $\bar{2}$ 0) surface. Therefore, the Ti-(0 0 0 1), Ti-(1 0 $\bar{1}$ 0) and the non-polar (1 1 $\bar{2}$ 0) surfaces should have comparatively lower surface energies.

3.5. Surface energy

The surface energies of low-index surfaces are calculated to further study the stabilities of surface structure. According to relative Refs. [10,14,35–36], the surface energy of symmetry nonpolar (1 1 $\bar{2}$ 0) surface is defined as:

$$\sigma_{\text{surface}} = (E_{slab} - N_{Ti}E_{TiB_2}^{bulk})/2A \qquad (6)$$

where E_{slab} and $E_{TiB_2}^{bulk}$ are the energies of the surface slab and bulk TiB$_2$, respectively; N_{Ti} is the number of Ti atom in the slab; A is the surface area; the factor 2 is due to two identical surfaces in the slab.

Meanwhile, the surface energy of a polar symmetric surface is a function of the chemical potential of each element in the compound. For the TiB$_2$ surface, it can be defined as:

$$\sigma_{\text{surface}} = (E_{slab} - N_{Ti}\mu_{Ti} - N_B\mu_B)/2A \qquad (7)$$

where E_{slab} is the total energy of the surface slab after complete relaxation; N_{Ti} and N_B are the numbers of the Ti and B atoms in the slab, respectively; μ_{Ti} and μ_B are the chemical potentials of Ti and B atoms, respectively.

Since it is hard to accurately calculate the chemical potential of each atom, we assume that the surface is in equilibrium with the bulk in the calculation. Therefore, the chemical potential of the bulk TiB$_2$ can be defined as:

$$\mu_{TiB_2}^{bulk} = \mu_{Ti} + 2\mu_B \qquad (8)$$

According to the thermodynamic stability of the compound, Eq.(9) can be obtained:

$$\mu_{TiB_2}^{bulk} = \mu_{Ti}^{bulk} + 2\mu_B^{bulk} + \Delta H_f^0(TiB_2) \qquad (9)$$

Combining Eqs. (8) with (9), the range of the B chemical potential thermodynamically is obtained as following:

$$\frac{1}{2}\Delta H_f^0(TiB_2) \leqslant \mu_B - \mu_B^{bulk} \leqslant 0 \qquad (10)$$

In conjunction with above all formulas and the calculation results in Table 1, the surface energies of low-index surfaces are calculated and shown in Fig. 6. The energy results illustrate the surface energies of

nonstoichiometric (0 0 0 1) and (1 0 $\bar{1}$ 0) surfaces are dependent on the chemical potential of B, while that of stoichiometric (1 1 $\bar{2}$ 0) surface is the opposite. With the increasing ($\mu_B - \mu_B^{bulk}$), the surface energies of B-(0 0 0 1) and (1 0 $\bar{1}$ 0) surfaces decrease and those of the Ti-(0 0 0 1) and (1 0 $\bar{1}$ 0) surfaces increase. Under the Ti-rich conditions, the stability of low-index surfaces of TiB$_2$ is following the sequence of Ti-(0 0 0 1) or Ti-(1 0 $\bar{1}$ 0) > (1 1 $\bar{2}$ 0) > B-(1 0 $\bar{1}$ 0) > B-(0 0 0 1), whereas under B-rich conditions it changes to B-(0 0 0 1) > (1 1 $\bar{2}$ 0) > B-(1 0 $\bar{1}$ 0) > Ti-(1 0 $\bar{1}$ 0) > Ti-(0 0 0 1). In general, the Ti-(0 0 0 1) and Ti-(1 0 $\bar{1}$ 0) surfaces are thermodynamically more favorable under Ti-rich conditions, while the B-(0 0 0 1) is thermodynamically more favorable under B-rich conditions.

According to the Wuff's theorem [39], the equilibrium crystal morphology should depend on the minimum total surface energy of the crystal. Thus, the equilibrium crystal morphology of TiB$_2$ particles should be hexagonal enclosed by the faces (0 0 0 1) and (1 0 $\bar{1}$ 0) based on our calculation result. This conclusion is consistent with our previous experimental results shown in Fig. 6b–d [40]. Moreover, it may be concluded that the transformation of morphologies of TiB$_2$ particles is indeed related to atomic concentration in the melt regarding the calculation results of surface energy. However, this opinion has required future experimental confirmation.

3.6. Work function

In order to understand the surface properties of the low-index surfaces of TiB$_2$ compound, we finally calculate the work functions of all above-considered surfaces. The work function (Φ) is defined as the minimum energy required to remove an electron at the Fermi level from the bulk region into the vacuum. Therefore, it can be obtained from the difference between the electrostatic potential in the vacuum region (D), and the Fermi energy (E_F) of the bulk [41]. For the surface slab calculations, a more accurate method is applied as presented in Refs. [42,43] to avoid the quantum-size effects. The schematic of this process is shown in Fig. 7. During the process, the planar averaged local electronic potential ($V_{\text{ave, }z}$) for the surface is shifted to match with the potential of corresponding bulk along the same direction. Then, the work function is obtained by D-E_F. Accordingly, the work function of each surface is calculated and follows the sequence of B-(0 0 0 1) (6.05 eV) > (1 1 $\bar{2}$ 0) (4.72 eV) > B-(1 0 $\bar{1}$ 0) (4.61 eV) > Ti-(0 0 0 1) (4.58 eV) > Ti-(1 0 $\bar{1}$ 0) (3.84 eV). Therefore, it can be clearly seen the B-(0 0 0 1) surface display the highest work function, which need future experimental confirmations.
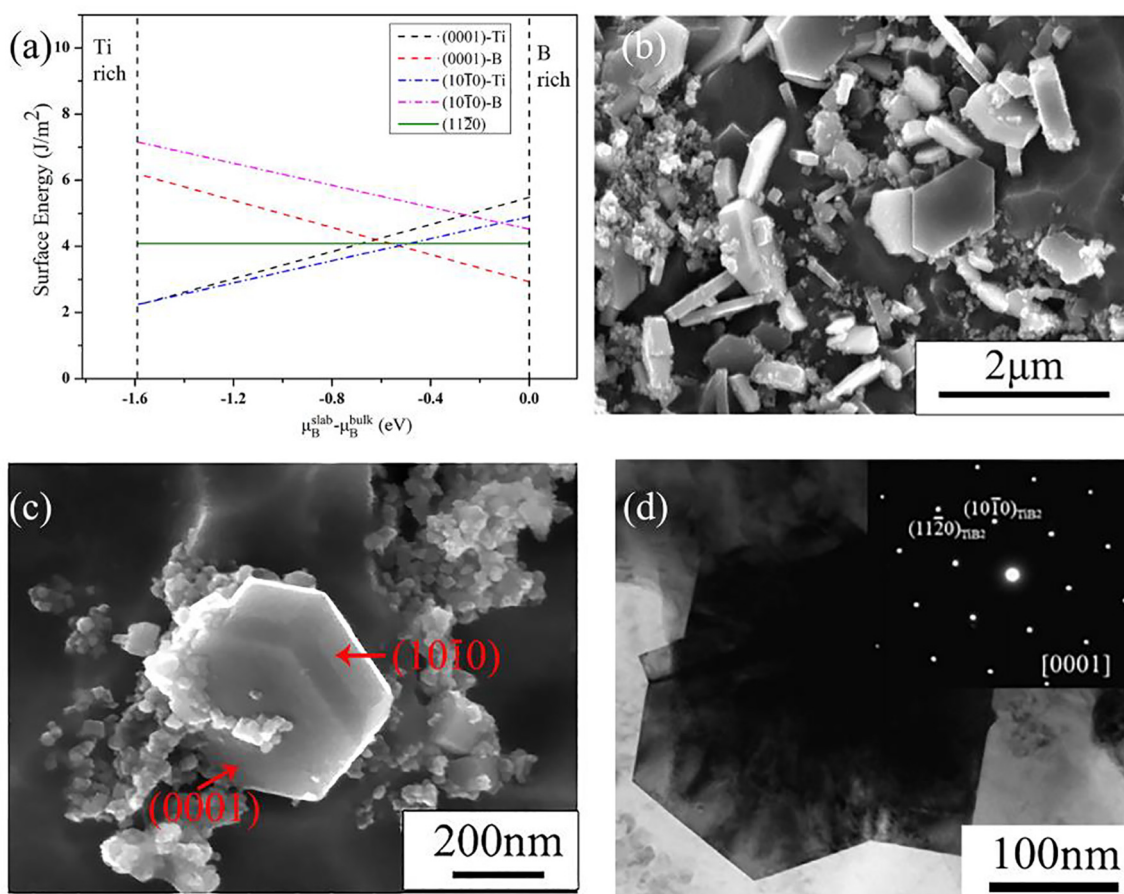
Fig. 6. Surface energy and morphology of TiB₂: (a) surface energies of low-index TiB₂ surfaces as a function of the chemical potential of B; (b) and (c) the morphology of TiB2 particle in Al matrix [40]; (d) TEM and the corresponding selected area diffraction (SAD) pattern of TiB₂ particle [40].
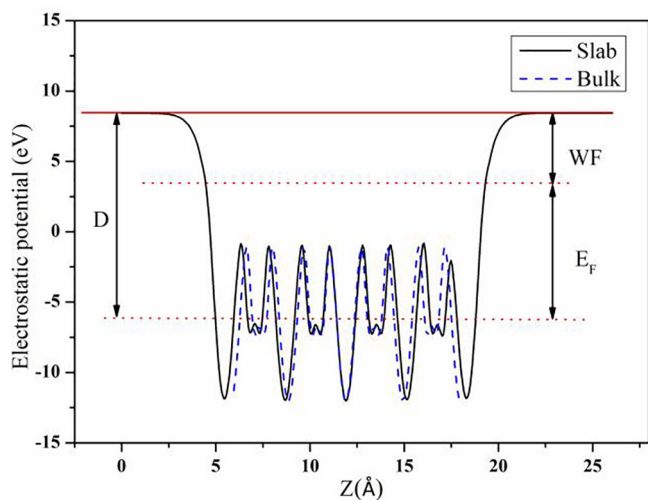
Fig. 7. Schematic of planar averaged potential for the surface slab and corresponding bulk (D is the vacuum level; WF is the work function; E_F is the Fermi energy of bulk).

4. Conclusions

The stability and work function of low-index surfaces of TiB₂ are studied using the first-principles calculations based on DFT. The structure relaxations mainly occur on the outermost two layers of surface structure. The changes in interlayer spacings in Ti-terminated $(0\,0\,0\,1)$ and $(1\,0\,\bar{1}\,0)$ surfaces are always less than those in B-terminated surfaces. Furthermore, the $(1\,1\,\bar{2}\,0)$ surface has minimal structure variation among all surfaces after relaxation. The charge accumulation mainly locates in the outmost layer, and the charge depletion in vacuum for Ti-terminated surfaces is much less than the corresponding B-terminated surfaces. Meanwhile, the charge transformation of non-polar $(1\,1\,\bar{2}\,0)$ surface is truly slight.

The calculated surface energies for polar $(0\,0\,0\,1)$ and $(1\,0\,\bar{1}\,0)$ surfaces are dependent on the chemical potentials of both Ti or B atoms in the surface slab. For the nonpolar $(1\,1\,\bar{2}\,0)$ surface, the calculated surface energy is $4.08\,\mathrm{J/m^2}$, which is independent of chemical potential. Moreover, the Ti-$(0\,0\,0\,1)$ and Ti-$(1\,0\,\bar{1}\,0)$ surfaces are thermodynamically more favorable under Ti-rich conditions, and the B-$(0\,0\,0\,1)$ surface is thermodynamically more favorable under B-rich conditions. This indicates that the morphologies of TiB₂ particles consisting of $(0\,0\,0\,1)$ and $(1\,0\,\bar{1}\,0)$ surfaces are related to the atomic concentration in the melt. Finally, the work function of all above-mentioned surfaces follow the sequence of B-$(0\,0\,0\,1)$ (6.05 eV) > $(1\,1\,\bar{2}\,0)$ (4.72 eV) > B-$(1\,0\,\bar{1}\,0)$ (4.61 eV) > Ti-$(0\,0\,0\,1)$ (4.58 eV) > Ti-$(1\,0\,\bar{1}\,0)$ (3.84 eV).

5. Data availability

The raw/processed data required to reproduce these findings cannot be shared at this time as the data also forms part of an ongoing study.

CRediT authorship contribution statement

Qian Wang: Conceptualization, Data curation, Formal analysis, Software, Writing - original draft. **Changzhi Liu:** Formal analysis, Software, Writing - review & editing. **Ruijuan Yao:** Software,

Visualization, Writing - review & editing. **Hong Zhu:** Methodology, Writing - review & editing. **Xiaomin Liu:** Methodology, Writing - review & editing. **Mingliang Wang:** Conceptualization, Formal analysis, Writing - review & editing. **Zhe Chen:** Conceptualization, Formal analysis, Funding acquisition, Writing - review & editing. **Haowei Wang:** Supervision, Writing - review & editing.

Declaration of Competing Interest

The authors declare that they have no known competing financial interests or personal relationships that could have appeared to influence the work reported in this paper.

Acknowledgments

Appendix A. Supplementary data

Supplementary data to this article can be found online at https://doi.org/10.1016/j.commatsci.2019.109356.

References

[1] R.G. Munro, Material properties of titanium diboride, J. Res. Natl. Inst. Stand Technol 5 (2000) 709–720.
[2] N. Kumar, G. Gautam, R.K. Gautam, Synthesis and characterization of TiB$_2$ reinforced aluminum matrix composites: a review, J. Inst. Eng. (India): Series D 97 (2016) 233–253.
[3] M.X. Zhang, P.M. Kelly, M.A. Easton, J.A. Taylor, Crystallographic study of grain refinement in aluminum alloys using the edge-to-edge matching model, Acta Mater. 53 (2005) 1427–1438.
[4] Z.Y. Ma, S.C. Tjong, High temperature creep behavior of in-situ TiB$_2$ particulate reinforced copper-based composite, Mater. Sci. Eng. A 284 (2000) 70–76.
[5] P. Li, Y. Wu, X. Liu, Controlled synthesis of different morphologies of TiB$_2$ microcrystals by aluminum melt reaction method, Mater. Res. Bull. 48 (2013) 2044–2048.
[6] J. Sun, X. Wang, L. Guo, et al., Synthesis of nanoscale spherical TiB$_2$ particles in Al matrix by regulating Sc contents, J. Mater. Res. 34 (2019) 1258–1265.
[7] A.A. Abdel-Hamid, S. Hamar-Thibault, R. Hamar, Crystal morphology of the compound TiB$_2$, J. Cryst. Growth 71 (1985) 744–750.
[8] M.E. Hyman, C. McCullough, C.G. Levi, Evolution of boride morphologies in TiAl-B alloys, Metall. Trans. A 22 (1991) 1647–1662.
[9] X. Gonze, B. Amadon, P.M. Anglade, et al., ABINIT: first-principles approach to material and nanosystem properties, Comput. Phys. Commun. 180 (2009) 2582–2615.
[10] P. Vajeeston, P. Ravindran, C. Ravi, Electronic structure, bonding, and ground-state properties of AlB$_2$-type transition-metal diborides, Phys. Rev. B 63 (2001) 0451151–04511512.
[11] M. Zhang, H. Wang, H. Wang, X. Zhang, T. Iitaka, Y. Ma, First-Principles prediction on the high-pressure structures of transition metal diborides (TMB$_2$, TM = Sc, Ti, Y, Zr), Inorg. Chem. 49 (2010) 6859–6864.
[12] M.M. Zhong, X.Y. Kuang, Z.H. Wang, P. Shao, L.P. Ding, X.F. Huang, Phase stability, physical properties, and hardness of transition-metal diborides MB$_2$ (M = Tc, W, Re, and Os): first-principles investigations, J. Phys. Chem. C 117 (2013) 10643–10652.
[13] T. Oguchi, Cohesion in AlB$_2$-type diborides: a first-principles study, J. Phys. Soc. Jpn. 71 (2002) 1495–1500.
[14] Y. Han, Y. Dai, D. Shu, Electronic and bonding properties of TiB$_2$, J. Alloy. Compd. 438 (2007) 327–331.
[15] M.L. Wang, The investigation of dependences of mechanical and electronic properties of TiB$_2$ on pressure using the first-principles method, Phys. Scr. 89 (2014) 1157021–11570212.
[16] Y. Han, Y. Dai, D. Shu, First-principles study of TiB$_2$ (0001) surfaces, J. Phys.: Condens. Matter 18 (2006) 4197–4205.
[17] K. Yamamoto, K. Kobayashi, H. Kawanowa, Difference in the outermost layer between TaB$_2$ (0001) and HfB$_2$ (0001), Phys. Rev. B 60 (1999) 15617–15620.
[18] R. Souda, E. Asari, H. Kawanowa, Low energy He+ ion scattering from HfB$_2$ (0001), TaB$_2$ (0001), WB$_2$ (0001), YB$_4$ (001), and YB$_6$ (001) surfaces, Surf. Sci. 414 (1998) 77–84.
[19] H. Kawanowa, K. Yamamoto, S. Otani, K. Kobayashi, Y. Gotoh, R. Souda, ARUPS study of graphitic boron terminated WB$_2$ (0001) surface, Surf. Sci. 463 (2000) 191–198.
[20] X. Zhang, X. Luo, J. Li, Structure and bonding features of ZrB$_2$ (0 0 0 1) surface, Comput. Mater. Sci. 46 (2009) 1–6.
[21] G. Kresse, J. Furthmueller, Efficient iterative schemes for ab initio total-energy calculations using a plane-wave basis set, Phys. Rev. B 54 (1996) 11169–11186.
[22] G. Kresse, J. Furthmuller, Efficiency of ab-initio total energy calculations for metals and semiconductors using a plane-wave basis set, Comput. Mater. Sci. 6 (1996) 15–50.
[23] G. Kresse, D. Joubert, From ultrasoft pseudopotentials to the projector augmented-wave method, Phys. Rev. B 59 (1999) 1758–1759.
[24] J.P. Perdew, K. Burke, M. Ernzerhof, Generalized gradient approximation made simple, Phys. Rev. Lett. 77 (1996) 3865–3868.
[25] R.P. Feynman, Forces in molecules, Phys. Rev. 56 (1939) 340–343.
[26] J.L. Murray, P.K. Liao, K.E. Spear, The B-Ti (Boron-Titanium) system, Bull. Alloy Phase Diagrams 7 (6) (1986) 550–555.
[27] W.M. Haynes, CRC Handbook of Chemistry and Physics, 92nd ed., CRC Press, 2011.
[28] J. Zhao, J.P. Lu, Pressure-induced metallization in solid boron, Phys. Rev. B 66 (2002) 092101.
[29] L. Topor, O.J. Kleppa, Enthalpies of formation of first-row transition-metal diborides by a new calorimetric method, J. Chem. Thermodyn. 17 (1985) 1003–1016.
[30] A. Waśkowska, L. Gerward, J.S. Olsen, Thermoelastic properties of ScB$_2$, TiB$_2$, YB$_4$ and HoB$_4$: experimental and theoretical studies, Acta Mater. 59 (2011) 4886–4894.
[31] D. Wearing, A.P. Horsfield, W. Xu, P.D. Lee, Which wets TiB$_2$ inoculant particles: Al or Al$_3$Ti? J. Alloy. Compd. 664 (2016) 460–468.
[32] J.L. Hoard, R.E. Hughes, The Beta-Rhombohedral Boron Structure, in: G.K. Gaulé (Ed.), Boron, Springer, Boston, MA, 1965.
[33] R. Liu, X. Yin, K. Feng, First-principles calculations on Mg/TiB$_2$ interfaces, Comput. Mater. Sci. 149 (2018) 373–378.
[34] H. Yan, W. Qun, S. Chang, A first-principle calculation of structural, mechanical and electronic properties of titanium borides, Trans. Nonferrous Met. Soc. China 21 (2011) 1627–1633.
[35] S.P. Sun, X.P. Li, H.J. Wang, First-principles investigations on the electronic properties and stabilities of low-index surfaces of L1$_2$-Al$_3$Sc intermetallic, Appl. Surf. Sci. 288 (2014) 609–618.
[36] Z. Jiao, Q.J. Liu, F.S. Liu, Structural and electronic properties of low-index surfaces of NbAl$_3$ intermetallic with first-principles calculations, Appl. Surf. Sci. 419 (2017) 811–816.
[37] C. Deng, B. Xu, P. Wu, Stability of the Al/TiB$_2$ interface and doping effects of Mg/Si, Appl. Surf. Sci. 425 (2017) 639–645.
[38] Y.F. Li, B. Xiao, G.L. Wang, Revealing the novel fracture mechanism of the interfaces of TiB$_2$/Fe composite from a first principles investigation, Acta Mater. 156 (2018) 228–244.
[39] G.C. Benson, D. Patterson, Note on an analytical proof of Wulff's theorem in three dimensions, J. Chem. Phys. 23 (1955) 670–672.
[40] J. Sun, X. Zhang, Y. Zhang, Effect of alloy elements on the morphology transformation of TiB$_2$ particles in Al matrix, Micron 70 (2015) 21–25.
[41] R. Tran, X.G. Li, J. Montoya, Anisotropic work function of elemental crystals, arXiv preprint arXiv:1902.07811, 2019.
[42] C.J. Fall, N. Binggeli, A. Baldereschi, Deriving accurate work functions from thin-slab calculations, J. Phys.: Condens. Matter 11 (1999) 2689–2696.
[43] H. Zhu, R. Ramprasad, The stability and work function of TaC$_x$N$_{1-x}$ alloy surfaces, J. Appl. Phys. 109 (2011) 0837191–0837196.